Journal of Materials Chemistry C

ROYAL SOCIETY OF CHEMISTRY

PAPER

View Article Online
View Journal | View Issue

Cite this: J. Mater. Chem. C, 2025, 13, 10139

Impact of crystallinity and local disorder on the luminescence properties of solvothermally synthesized $LuPO_4:Pr^{3+}$ nanocrystals†

Sanu Bifal Maji, *[a] Alexander Vanetsev, [a] Vitali Nagirnyi,[a] Kirill Chernenko,[b] Eduard Feldbach,[a] Jekaterina Kozlova,[a] Hugo Mändar,[a] Ivo Romet, [a] Mihkel Rähn[a] and Marco Kirm[a]

Received 28th January 2025,
Accepted 7th April 2025

DOI: 10.1039/d5tc00391a

rsc.li/materials-c

In this study, we present the solvothermal synthesis of $LuPO_4:Pr^{3+}$ (1%) nanocrystals in a dimethyl sulfoxide–water solvent system. The as-prepared nanocrystals exhibit a relatively high degree of crystallinity, along with significant short-range disorder, particularly in the anionic sublattice, as revealed by XRD and Raman spectroscopy data. Low temperature luminescence spectroscopy under VUV excitation showed that this disorder hinders the energy transfer from the host lattice to the Pr^{3+} ions, resulting in the absence of the $4f^15d^1 \rightarrow 4f^2$ emission under high energy excitation. Thermal annealing of as-prepared nanocrystals significantly reduces the degree of local disorders enhancing UV-C luminescence in the 4.4–5.5 eV range by improving energy transfer processes from the $LuPO_4$ host to Pr^{3+} ions. Time-integrated luminescence spectra reveal up to a five-fold increase in UV-C emission intensity after annealing. UV-C emissions due to Pr^{3+} ions in $LuPO_4$ are efficiently excited in the deep intrinsic absorption region at 45 eV, which simulates the energy conversion process for radiotherapy applications. Time-resolved studies identify two types of Pr^{3+} ions. One group consists of strongly perturbed ions near the nanoparticle surface, influenced by structural imperfections, while the other includes weakly perturbed ions located in the bulk. These results highlight the critical role of local structural imperfections almost undetectable by XRD in energy transfer processes involving the host lattice.

1. Introduction

Recently, research efforts to improve the efficiency of radiotherapy by using rare-earth luminescent materials have gained increased interest. Radiotherapy is one of the most widely used techniques to treat various tumors, such as skin, prostate, lung, and cervix carcinomas.[1] In radiotherapy, ionizing radiations such as X-rays, electrons, and particle beams transfer energy into cells, generating reactive oxygen species (ROS) (*e.g.*, singlet oxygen).[2,3] When the ROS concentration overwhelms the body's antioxidant defense mechanisms, oxidative stress leads to cellular damage.[4] However, these treatment techniques are limited by two factors: the maximum radiation dose that can be delivered to tumorous cells without significantly damaging adjacent normal cells, and the presence of oxygen and other compounds suitable for ROS generation.[5] A promising approach to overcome these limitations is the use of UV-C photon-emitting materials to induce additional cellular damage.[1,5] UV-C radiation can directly be absorbed and can damage cellular DNA or indirectly increase ROS generation.[3] For instance, Miwa *et al.* demonstrated UV-C radiation-induced destruction of human pancreatic carcinoma cells, showing a 70% cell death rate under a 25 J m^{-2} UV-C dose.[6] This highlights the potential of UV-C photon-emitting materials for improving radiotherapy efficiency.

Several studies have explored rare-earth luminescent materials for their ability to emit high-energy photons and their suitability in radiotherapy. For example, Vistovskyy *et al.* investigated Pr^{3+} and Eu^{3+}-doped phosphates, demonstrating their efficient UV photon emission and the critical role of crystallinity and particle size in determining luminescence performance.[7] Building on these findings, $LuPO_4:Pr^{3+}$, known for its promising luminescence properties, was chosen as the focus of the present work. The ability of such materials to function as UV-C photon emitters under high-energy excitation makes them suitable candidates for enhancing radiotherapy outcomes.[8] To achieve effective delivery and performance, nanoparticles of high-density compounds like $LuPO_4:Pr^{3+}$ must be dispersible and stable in colloidal solutions. This allows their transportation to the targeted sites using

[a] Institute of Physics, University of Tartu, W. Ostwald Str. 1, 50411 Tartu, Estonia. E-mail: sanu.bifal.maji@ut.ee
[b] MAX IV Laboratory, Lund University, P.O. Box 118, SE-22100, Lund, Sweden

† Electronic supplementary information (ESI) available. See DOI: https://doi.org/10.1039/d5tc00391a

nanocarrier molecules (*e.g.*, polymeric nanoparticles, micelles, liposomes, *etc.*) modified with ligands that specifically recognize tumor cell receptors.[9,10] The overall size of the system (including the nanoparticles and carrier molecules) should remain as small as possible, typically within the range of 10 to 200 nm.[11] Moreover, smaller carrier molecules result in higher cell uptake compared to larger, micro-sized carriers, allowing for better access to cellular and intracellular targets.[12] A larger surface area-to-volume ratio in smaller particles also leads to faster and more efficient release of the active agents at the targeted site.[13]

Achieving optimal luminescence performance for nanoparticles in such nanocarriers depends heavily on their crystallinity.[14] Local disorder, especially in the form of structural defects and short-range and long-range disordering at the nanoscale, can have significant effects on the luminescence properties.[15] In many cases, as-prepared nanoparticles exhibit high levels of short-range disorder, particularly in the anionic sublattice.[14,16] This local disorder can lead to the distortion of the unit cell, impairing energy transfer processes and reducing luminescence efficiency. Surface defects and imperfections, such as dangling bonds or absorbed species, can also serve as quenching centers, further hindering the occurrence of radiative transitions.

Annealing at high temperatures is a well-known method to reduce local disorders and improve the crystallinity of materials.[7,17] This process not only aids in recrystallization but also reduces the structural imperfections, facilitating better energy transfer from the host lattice to the Pr^{3+} ions. By minimizing the influence of these local disorders, the overall luminescence efficiency of the nanoparticles can be significantly enhanced, making them more suitable for practical applications in radiotherapy. In this work, we explore a novel solvothermal synthesis method to produce $LuPO_4$:Pr^{3+} nanocrystals in a dimethyl sulfoxide (DMSO) water solvent system. A doping concentration of 1% Pr^{3+} was selected based on previous studies, which demonstrated that lower doping levels (*e.g.*, 0.1%) result in inefficient energy transfer, whereas higher concentrations (*e.g.*, 3%) lead to concentration quenching.[18] This ensures an optimal balance between strong luminescence and minimal quenching losses. We examine how annealing affects their structure, size, and luminescence properties, paying particular attention to the effects of local disorder on luminescence performance. Specifically, we compare the as-prepared nanocrystals, which exhibit significant local disorders, with annealed nanocrystals that show enhanced crystallinity and improved luminescence.

2. Materials and Methods

$LuPO_4$:Pr^{3+} (1%) nanocrystals were synthesized by the solvothermal method in DMSO–water media. The reagents used for this synthesis were $Lu(NO_3)_3{\cdot}6H_2O$ (Sigma-Aldrich, 99.9% purity), $Pr(NO_3)_3{\cdot}6H_2O$ (Sigma-Aldrich, 99.99% purity), $(NH_4)_2HPO_4$ (Sigma-Aldrich, >99% purity), DMSO (Honeywell Riedel-de-Haën, 99.7% purity) and Milli-Q water.

In our typical synthesis process, 9.9 mmol solution of $Lu(NO_3)_3$ and 0.1 mmol (1%) solution of $Pr(NO_3)_3$ were prepared in 20 mL and 5 mL of DMSO–water mixed solvent, respectively. The solvent used for the synthesis was a mixture of DMSO and Milli-Q water in different ratios, namely, for the sample L1 – 30% DMSO : 70% water, L2 – 50% DMSO : 50% water, respectively. Both solutions were mixed together using a magnetic stirrer for 15 minutes. Simultaneously 10 mmol solution of $(NH_4)_2HPO_4$ was prepared in 25 mL of DMSO–water solvent. The $(NH_4)_2HPO_4$ solution was added to the above solution of rare earth nitrates in a dropwise manner under vigorous stirring for 30 minutes. The resultant mixture was transferred to the 100 mL Teflon autoclave, treated at 200 °C for 3 hours, and then cooled down to room temperature. The sample was then centrifuged at 10 000 rpm (Heraeus Multifuge centrifuge) for 10 minutes, and the transparent supernatant was discarded. The precipitate was washed several times with double distilled water and ethanol and then dried at 100 °C for 2 hours. The powders obtained with two different DMSO ratios (L1 and L2) will be further referred to as ''as-prepared L1'' and ''as-prepared L2''. Half of the synthesized powders were then annealed at 1000 °C in an argon atmosphere for 2 hours and will be further referred to as ''annealed L1'' and ''annealed L2'', respectively. An argon gas atmosphere was used during annealing to prevent the oxidation of Pr^{3+} to Pr^{4+}. As-prepared and annealed powders were then studied using various analytical and spectroscopic techniques described below.

The phase composition of samples was characterized by X-ray diffraction (XRD). Diffraction patterns were measured using Bragg–Brentano optics on an X-ray diffractometer SmartLab™ (Rigaku, Japan) working at source power of 8.1 kW (Cu Kα radiation, λ = 0.1540598 nm). The X-ray true size of crystallites was calculated by Voigt analysis of peak shapes assuming a cylindrical shape model.[19] The used instrumental broadening of reflections was based on measurements of the standard reference material SRM-660 (LaB_6). Cell parameters were calculated using the whole powder X-ray diffraction pattern fitting algorithm.[20] Data from databases PDF-2 (version 2023, from International Center of Diffraction Data, USA) and ICSD (version 2021, from FIZ Karlsruhe, Germany) were used for crystalline phase identification and calculation of diffraction patterns, respectively. For studying the crystallinity and vibrational spectra of the $LuPO_4$:Pr^{3+} nanocrystals, Raman spectroscopy was applied. A micro-Raman setup (Renishaw in Via) equipped with a continuous multi-line argon laser (Stellar-Pro) operating at 514 nm and an optical DM Microscope (Leica Microsystems) were used for the measurements of Raman scattering spectra. The detailed description of the experimental setup has been presented elsewhere.[21] A FEI Titan Themis 200 Cs-corrected (scanning) transmission electron microscope (STEM) operated at 200 kV in the STEM mode was used to study the morphology of as-prepared and annealed $LuPO_4$:Pr^{3+} nanocrystals. High-angle annular dark-field (HAADF) and bright-field (BF) images were simultaneously captured from the same locations on the sample. For the STEM analysis, a particle suspension in 2-propanol was drop cast onto a carbon film-covered 300-mesh copper TEM grid.[22,23]

Time-integrated (TI) luminescence spectroscopy of as-prepared and annealed $LuPO_4$:Pr^{3+} nanocrystals in the

temperature range of 6–300 K was carried out using the FinEstBeAMS beamline located at the 1.5 GeV storage ring of the MAX IV synchrotron radiation laboratory. The low-temperature measurement (6.8 K) was chosen to minimize thermal quenching, enabling a more detailed analysis of intrinsic energy transfer mechanisms and spectral characteristics, while the room-temperature measurement (300 K) provides insight into the material's performance under practical conditions, particularly for potential applications in scintillation and biomedical applications. The detailed description of the beamline design, its performance and photoluminescence setup used can be found in ref. 24–26. The multi-bunch operation mode of a 1.5 GeV storage ring was applied in recording the TI luminescence spectra using an Andor CCD camera (Newton DU970P-BFV) in the spectral range of 200–700 nm and a Hamamatsu photon counting head H8259–01 sensitive in a spectral range of 200–900 nm mounted in two different exit ports of an Andor Shamrock (SR-303i) 0.3 m spectrometer. The typical spectral resolutions in measuring the emission spectra were 8.2 and 3.1 nm using the photon counting head and CCD detector, respectively. The time-integrated excitation spectra were obtained by recording the emission spectra for each exciting photon energy using the CCD camera. During data analysis, the desired excitation spectrum was generated allowing for detailed analysis by integrating intensity over a specific wavelength (energy) range of the selected emission band. Moreover, all spectra are corrected for the sensitivity of the detection channel.

The time resolved luminescence studies were performed only at 6–7 K using an ultra-fast Hamamatsu R3809U-50 MCP-PMT detector in the single-bunch operation mode of the 1.5 GeV storage ring at MAX IV. The time resolution of the detection system, *i.e.* an instrumental response function (IRF), was determined to be 174 ps. The details of the time-resolved luminescence method implemented at FinEstBeAMS and the technical information of equipment in use can be found in ref. 27 and 28. The photon flux of the beamline was recorded with an AXUV-100G photodiode for normalizing excitation spectra to the same amount of incident photons. In all experiments the slit width of the primary monochromator was set to 150 μm, which corresponded to the spectral resolution better than 4 meV at 10 eV (*i.e.*, a resolving power of ~2500) of the exciting photon beam.[25]

3. Results and discussion

3.1. Phase composition and morphology of $LuPO_4:Pr^{3+}$ (1%) powders

The XRD phase analysis of solvothermally synthesized powders showed that all observed reflections (Fig. 1) for both as-synthesized and annealed samples of L1 and L2 can be indexed to the tetragonal phase of $LuPO_4$ (PDF-2 file number 84-337 and ICSD collection code 162336, space group $I4_1/amd$). This demonstrates that the solvothermal synthesis method can successfully produce the tetragonal phase of $LuPO_4$. Furthermore, the solvothermal synthesis method offers an advantage over water-based techniques, as it facilitates the formation of hydrated rare-earth phosphates, which typically crystallize in a

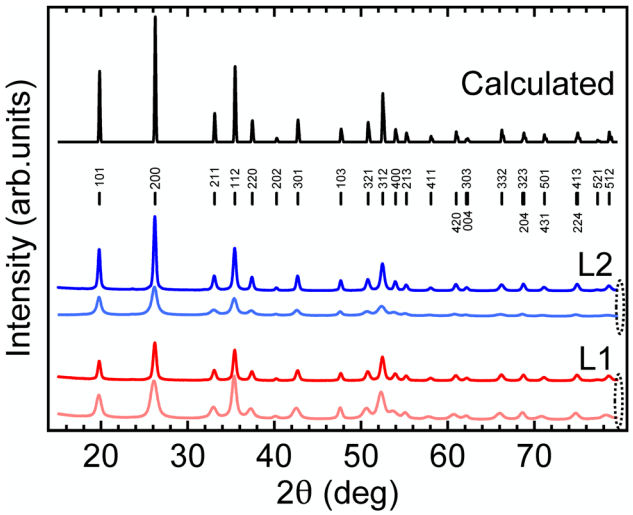

Fig. 1 XRD patterns of as-prepared (lower curve) and annealed (upper curve) $LuPO_4:Pr^{3+}$ (1%) powder synthesized in L1 (30% DMSO–70% water) solvent and L2 (50% DMSO–50% water) solvent. The calculated diffraction pattern including the indices of reflections of tetragonal $LuPO_4$ is shown at the topmost part of the figure.

hexagonal crystal structure due to the incorporation of water molecules.[29–31] The cell parameters of the as-prepared $LuPO_4:Pr^{3+}$ samples (Table 1) were considerably larger compared to the ones of undoped $LuPO_4$ (a = 0.67827, c = 0.59467).[32] This can be explained by a larger ionic radius of Pr^{3+} (127 pm) compared to that of Lu^{3+} (98 pm) for the VIII coordination.[33] The estimation of the crystallite shape and size was performed using a cylindrical model, which accounts for the anisotropic growth of the crystallites. This anisotropy, evident from the XRD analysis, reflects differences in the crystallite size along specific crystallographic directions. The Voigt analysis of XRD peak shapes showed that the mean diameters of the as-prepared $LuPO_4:Pr^{3+}$(1%) samples (L1 and L2) were approximately 9 and 10 nm, respectively, with the size along the [001] direction being slightly larger than that along the [100] and [010] directions (Table 1).

Annealing of $LuPO_4:Pr^{3+}$samples (annealed L1 and L2) increased the size of crystallites up to 17 and 21 nm, respectively, and decreased the degree of anisotropy (see Tables 1 and 3). After annealing, a decrease in cell parameters was observed, but the final values were still significantly larger in comparison to the undoped $LuPO_4$. This decrease of cell parameters may be related to a lower disorder rate in the annealed samples

Table 1 The list of the samples studied, their cell parameters a and c, X-ray mean true sizes ($\langle 2r\rangle$ and $\langle h\rangle$) of crystallites in [100] and [001] directions that correspond to the average diameter and length of the crystallites by assuming their cylindrical shape. The values in parentheses are standard deviations relative to the last significant digit of a parameter or size

Type of the sample	a, nm	c, nm	$\langle 2r\rangle_{100}$, nm	$\langle h\rangle_{001}$, nm
L1 (30% DMSO–70% water)	0.6824(2)	0.5970(2)	9(1)	19(2)
Annealed L1 (1000 °C)	0.6800(2)	0.5965(2)	19(1)	25(2)
L2 (50% DMSO–50% water)	0.6825(2)	0.5972(2)	10(1)	14(2)
Annealed L2 (1000 °C)	0.6800(2)	0.5965(2)	23(1)	27(2)

compared to that in as-prepared samples. It is well-known that local disorder can lead to the dilation of the unit cell[34] and synthesis at relatively low temperature could result in the formation of a disordered phase. On the other hand, there is no impurity phase contribution observed in the XRD patterns, as well as no sign of a significant amount of an amorphous phase. Thus, we can assume that the samples possess long-range ordering, while short-range disorder in the first and/or second coordination sphere may be present.

In order to study structural peculiarities, we compared the results of XRD studies with those of Raman spectroscopy, which is specifically sensitive to the short-range ordering.[35] The unit cell of tetragonal $LuPO_4$ consists of Lu^{3+} at the D_{2d} lattice site, which is 8-fold coordinated by oxygen atoms (Fig. 2), forming a dodecahedron with triangular planes and providing a single site for the isovalent Pr^{3+} dopant ion.[36] According to the literature data, there are twelve Raman active vibrational modes in the $LuPO_4$ structure.[37] All these vibrational modes, except the one at 321 cm^{-1}, are well-observed in both annealed $LuPO_4$:Pr^{3+} samples (see Fig. 3 and Table 2), however, these are absent in the as-prepared $LuPO_4$:Pr^{3+} samples, which confirms the hypothesis of short-range disordering. The nature of this disorder requires additional structural studies, but we tentatively suggest that it is related to the displacement (most likely rotation) of the PO_4 groups in the lattice. Another possibility is the protonation of the PO_4 group, which has been observed in the case of YPO_4 microwave-hydrothermal synthesis and has been shown to cause the displacement of oxygen atoms in the lattice and lowering the symmetry of the PO_4 group.[38] Given the light weight of oxygen, such displacement does not strongly affect the XRD pattern (apart from a slight increase of the cell parameters), but might have a significant effect on Raman modes, as all of them are related to the vibrations involving oxygen atoms. Our hypothesis is that random shifts of oxygen atoms in the lattice lead to full disappearance of Raman bands similar to an amorphous phase,

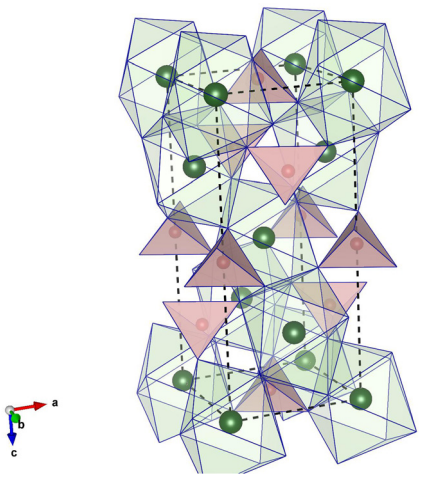

Fig. 2 The crystal structure model of the tetragonal unit cell of $LuPO_4$ in polyhedral presentation: green atoms – Lu, red atoms – P; oxygen atoms are located at the vertices of polyhedra, but not presented for the sake of the image clarity. The figure has been prepared using VESTA software.

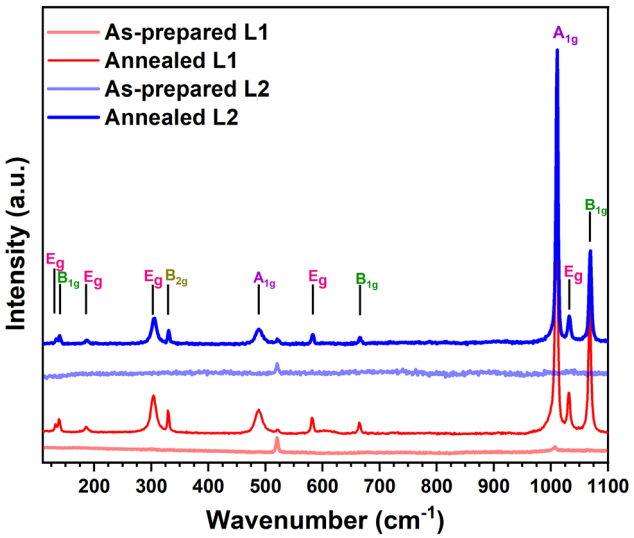

Fig. 3 Raman spectra of the as-prepared and annealed $LuPO_4$:Pr^{3+} nanocrystals recorded at 300 K. The band at 520 cm^{-1} in the spectra of as-prepared samples is related to the silicon substrate.

Table 2 Experimentally determined optical phonon modes of the annealed L1 and L2 nanocrystals and their assignments to the specific vibrations. The Raman mode $B_{1g}(2)$ is absent in the experimental spectrum

S. No	Raman modes	Experimental results of this work (cm^{-1})	Experimental data from ref. 37 (cm^{-1})
1.	$E_g(1)$	133.2	133
2.	$B_{1g}(1)$	139.4	139
3.	$E_g(2)$	186.4	187
4.	$E_g(3)$	306.2	306
5.	B_{2g}	330.4	331
6.	$A_{1g}(1)$	488.5	490
7.	$E_g(4)$	582.7	582
8.	$B_{1g}(3)$	665.4	665
9.	$A_{1g}(2)$	1010.9	1010
10.	$E_g(5)$	1031.9	1031
11.	$B_{1g}(4)$	1069.4	1069

though the XRD pattern shows long ranged ordering in the material. The XRD measurement is more sensitive to the contribution of heavy Lu atoms, resulting in well-defined XRD patterns.

The STEM images of as-prepared $LuPO_4$:Pr^{3+} samples demonstrate elongated nanoparticles of irregular shape (see Fig. 4(1(a) and 2(a)). Such shape is in good correlation with the results of XRD pattern analysis showing the anisotropic growth along the [001] direction. Although the irregular appearance suggests imperfect formation of defined facets, this may be partly due to the limited resolution of the STEM images (Fig. 4(1(b), (c) and 2(b), (c)), as some facets can be discerned. The growth of nanoparticles proceeds along the most energetically favorable crystallographic direction, [001], which is typical for tetragonal $LuPO_4$ crystals. The observed shapes suggest that primary nuclei grew preferentially along the [001] direction and stacked along this axis to form the nanoparticles visible in the STEM images. Quantitative size distribution analysis of the

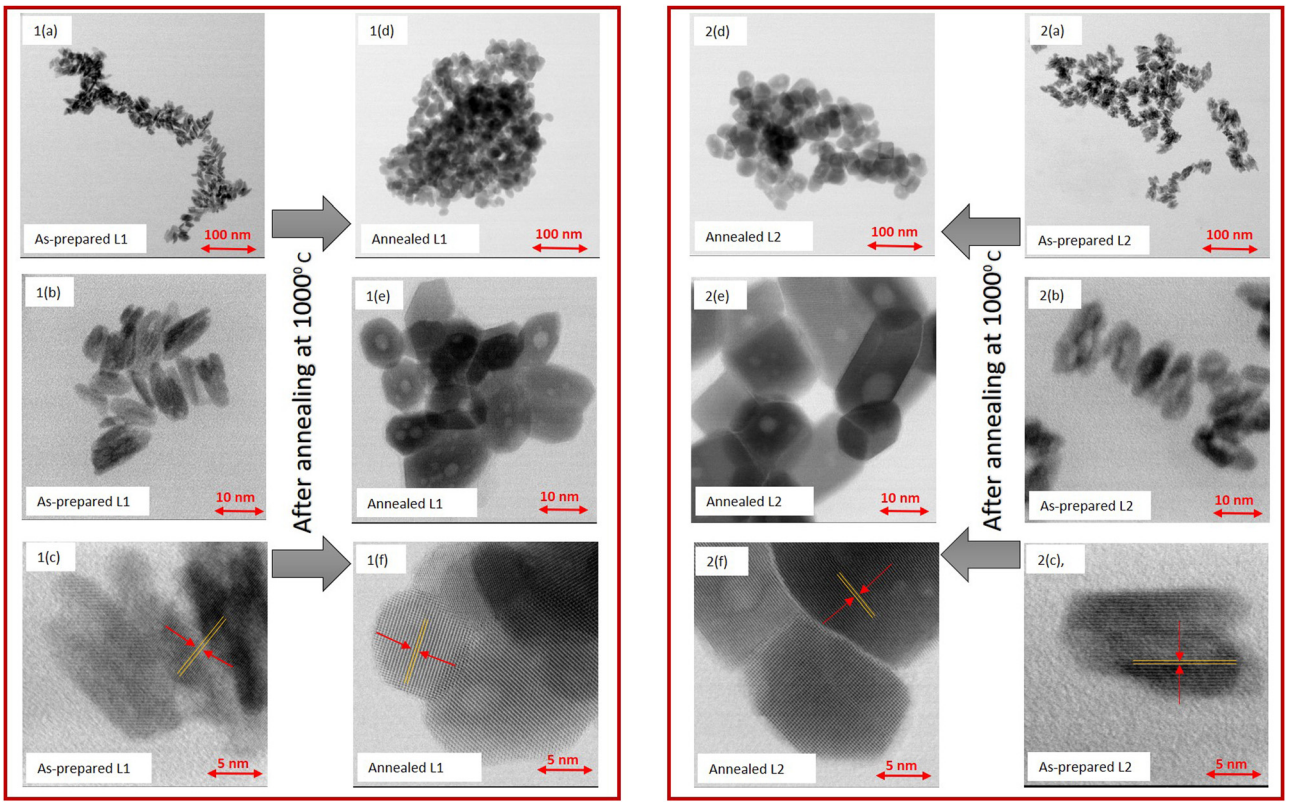

Fig. 4 The first row [1(a), 1(d), 2(d) and 2(a)] STEM images are of different $LuPO_4$:Pr^{3+} (1%) nanocrystal families displaying uniformity of the particles. The middle row images [1(b), 1(e), 2(b) and 2(e)] are high resolution TEM images for smaller $LuPO_4$:Pr^{3+} (1%) nanocrystal agglomerates. The bottom row [1(c), 1(f), 2(c) and 2(f)] shows high-resolution STEM images taken at a 5 nm resolution, with visible lattice fringes indicating crystallinity.

STEM images of over 400 nanoparticles for both as-prepared $LuPO_4$:Pr^{3+} samples is shown in Fig. S1 in the ESI† data. Due to the anisotropic nature of the formed nanoparticles, it was impossible to calculate a single valid mean size from the STEM images. Thus, the mean width and mean length of the synthesized nanoparticles, as well as their degree of anisotropy, were estimated. Additionally, we had calculated the mean quadratic value of the mean width and mean length in order to compare this single value with the average crystallite size obtained from the XRD patterns (Table 3). The mean quadratic values for the as-prepared L1 and L2 samples are 12 ± 2 nm and 16 ± 1 nm, respectively. The degree of anisotropy between the mean length and the mean width of as-prepared nanoparticles is 2.50 and 3.56 for L1 and L2, respectively.

There is a good correlation between the mean quadratic values of particle dimensions calculated from STEM images and the average crystallite size obtained from XRD analysis (Table 3). This allows us to suggest that the degree of crystallinity is already rather high in as-prepared $LuPO_4$:Pr^{3+} nanoparticles. However, this contradicts the results of Raman spectroscopy, which shows no bands in the recorded spectra of such nanoparticles. Thus, as mentioned above, it is possible that the long-range order in as-prepared nanoparticles, deduced from the XRD analysis, is accompanied by the local disorder, most likely in the anionic sublattice, revealed in the Raman shift spectra. After annealing, the nanoparticles become relatively isotropic (the degree of anisotropy is 1.27–1.23) and their mean particle sizes and crystallinity increase. Also, the annealed nanoparticles become well-shaped with clearly defined facets (see Fig. 4(1(e) and 2(e)). In this process, nanoparticles tend to form densely sintered agglomerates with thin

Table 3 Morphology parameters of the as-prepared and annealed $LuPO_4$ samples derived from XRD and STEM analyses

		STEM size (400 particles)					
S. No.	Sample name	Mean width (W) (nm)	Mean length (L) (nm)	Mean quadratic value (nm) $\sqrt{\frac{(W)^2+(L)^2}{2}}$	Degree of anisotropy using STEM (length/width)	X-ray mean true diameter of cylindrical shape crystallites (nm) $\langle 2r \rangle$	Degree of anisotropy using XRD
1.	As-prepared L1	6 ± 1.0	16 ± 2.5	12 ± 2	2.50	9	1.85
2.	Annealed L1	17 ± 1.6	21 ± 2.3	19 ± 2	1.27	19	1.38
3.	As-prepared L2	6 ± 0.8	22 ± 2.0	16 ± 1	3.56	10	1.42
4.	Annealed L2	22 ± 2.2	27 ± 2.6	25 ± 3	1.23	23	1.17

low-angle boundaries. This improvement is due to the recrystallization and Ostwald ripening during annealing. The mean quadratic values between the mean width and the mean length of the annealed nanoparticles, calculated using the same procedure as for the as-prepared nanoparticles (as shown in Fig. S1, ESI†), are 19 ± 2 nm and 25 ± 3 nm, respectively (Table 3). These values are quite comparable to the sizes calculated from the XRD patterns, showing the increase in crystallinity and possibly also a decrease in anisotropy.

The evolution of nanoparticle morphology during annealing at high temperature in an inert atmosphere is qualitatively different from solvothermal growth. During the solvothermal synthesis, particles grow intensively along one direction with unrestricted mass flow from the solution. However, the low temperature limits recrystallization and the formation of well-defined facets, resulting in nanoparticles with numerous structural imperfections. In contrast, thermal annealing in an inert atmosphere promotes more isotropic and slower growth due to limited mass flow between particles, while the significantly higher processing temperature (1000 °C) drives an intensive recrystallization process. This process reduces the concentration of structural imperfections and enhances the overall crystallinity of the calcined nanoparticles. Another important aspect after annealing is the formation of dense agglomerates of nanoparticles with thin low-angle borders between them. For many processes such agglomerates can act as a single bulk material, as grain boundaries are thin and easily penetrable. However, in the applications where well-dispersed nanoparticles are required, as in biological or optoelectronic systems, the agglomeration can be a limiting factor. Potential strategies to mitigate this effect include the surface modification, the calcination in matrices, or the use of the surfactants during post-processing.[39,40] While this study focuses on structural and luminescence properties, future work could explore these methods to improve particle dispersion for the practical applications demanding the use of stable colloids of nanoparticles.

3.2. Photoluminescence study of the as-prepared and annealed $LuPO_4$:Pr^{3+} (1%) nanocrystals under synchrotron radiation excitation

The luminescence properties of $LuPO_4$:Pr^{3+} nanocrystals are largely influenced by the interaction between the electronic states of the host material and Pr^{3+} impurity ions. This interaction results in various relaxation processes that govern the energy transfer from the host to rare earth ions. Using the P. Dorenbos methodology, which applies to all rare earth elements, one can predict the energy level scheme of Pr^{3+} in $LuPO_4$, showing the positions of the 4f and 5d energy levels in the electronic band structure of the host[41] (see Fig. 5). As shown in Fig. 5, a strong crystal field of $LuPO_4$ positions the 5d energy bands slightly below the 4f $^1S_0$ energy level, enabling dipole and parity-allowed interconfigurational $4f^15d^1 \rightarrow 4f^2$ radiative transitions, which are responsible for the broad-band Pr^{3+} emission observed usually in the UV-C spectral region. In the case of close positions of the 5d term and $^1S_0$ level, narrow emission lines due to the $4f^2 \rightarrow 4f^2$ transitions can also be observed both through the direct intra-center excitation and through the host excitation *via* energy transfer processes populating the respective levels.[42] Furthermore, intrinsic emissions, such as broad-band self-trapped exciton emission peaked near 3 eV, can also be present in $LuPO_4$ under the host excitation in the excitonic and fundamental absorption region.[43,44]

As an example of overview emission spectra recorded for the synthesized $LuPO_4$:Pr^{3+} samples, a spectrum recorded under the excitation of the annealed L1 powder with 45 eV photons at 6.5 K is shown in Fig. 6. Indeed, strong emission bands from 5.5 to 4.4 eV are observed in the UV region that occur due to the parity allowed inter-configurational $4f^15d^1 \rightarrow {}^3H_4$, $^3H_5$, $^3H_6$ and $^3F_{2,3,4}$ ($4f^2$) radiative transitions in Pr^{3+} ions adhering to the spin selection rule ($\Delta S = 0$) because the initial excited $4f^15d^1$ state is triplet. The corresponding emission maxima in our synthesized $LuPO_4$:Pr^{3+} (1%) nanocrystals are located at 5.31 eV (233 nm), 5.06 eV (245 nm), 4.71 eV (263 nm), and 4.56 eV (271 nm), which are in good agreement with the already reported emission bands in $LuPO_4$:Pr^{3+} materials.[17,18] The non-elementary emission bands near 4.5 eV (271 nm) formed from various overlapping sub-bands spectrally better resolved at low temperatures (see Fig. 5 and 6) are due to the transitions to the $^3F_{2,3,4}$ multiplet. Moreover, few relatively weak narrow bands that can be distinguished in the visible spectral region are connected with the $4f^2 \rightarrow 4f^2$ transitions of Pr^{3+} ions. Remarkably, no sign of self-trapped exciton emission could be detected in the spectra. These circumstances allowed us to focus on a detailed study of the UV $4f^15d^1 \rightarrow 4f^2$ emission of synthesized nanoparticles, highly promising for radiotherapy applications. Excitation by high-energy 45 eV photons results in intense UV-C emissions and these conditions simulate the energy conversion process needed for improvement of radiotherapy efficacy.

3.2.1. Time-integrated photoluminescence excitation spectra of Pr^{3+} emission. To the best of our knowledge, as-prepared $LuPO_4$ nanocrystals studied in the present work are the first described example of the material that according to XRD analysis exhibits crystalline structure with tetragonal lattice symmetry but lacks any vibrational bands in its Raman spectrum. Therefore, it was important to study how the suggested high degree of short-range disorder in crystal lattice affects the luminescence properties and energy transfer process in $LuPO_4$:Pr^{3+}. The Pr^{3+} $4f^15d^1 \rightarrow 4f^2$ emission demonstrates a well-resolved complicated spectrum, which allows for the reliable attribution of the observed lines to the transitions from the excited $4f^15d^1$ state to various Stark components of the split Pr^{3+} ground state. This analysis is based, for example, on the level diagram provided in ref. 45, as has also been done in previous studies.[46] TI photoluminescence (PL) excitation spectra of one of these emission bands peaking at 5.06 eV and related to the $4f^15d^1 \rightarrow {}^3H_5$ transition, recorded for both as-prepared and annealed $LuPO_4$:Pr^{3+} (1%) nanocrystals at 6.8 K with the CCD detector, are shown in Fig. 7.

During the post-measurement analysis, the excitation spectra of the $4f^15d^1 \rightarrow {}^3H_5$ transition were obtained by integrating the emission recorded using the CCD detector in the energy range from 4.9 eV to 5.1 eV. The features of the excitation spectra in the range from 5.4 eV to 7.5 eV correspond to the intra-center

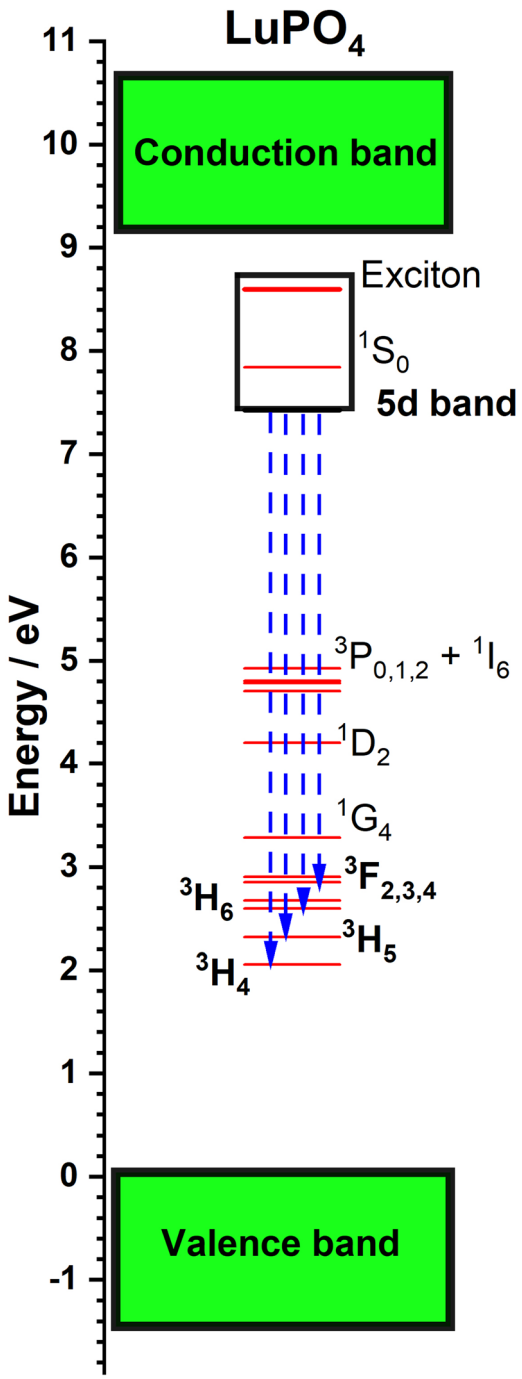

Fig. 5 Schematic representation of the fundamental electronic structure of $LuPO_4$:Pr^{3+}, based on P. Dorenbos' methodology.[17,41] The host near-edge energy bands, impurity levels and the Pr^{3+} $4f^15d^1 \rightarrow 4f^2$ transitions (blue arrows) are illustrated.

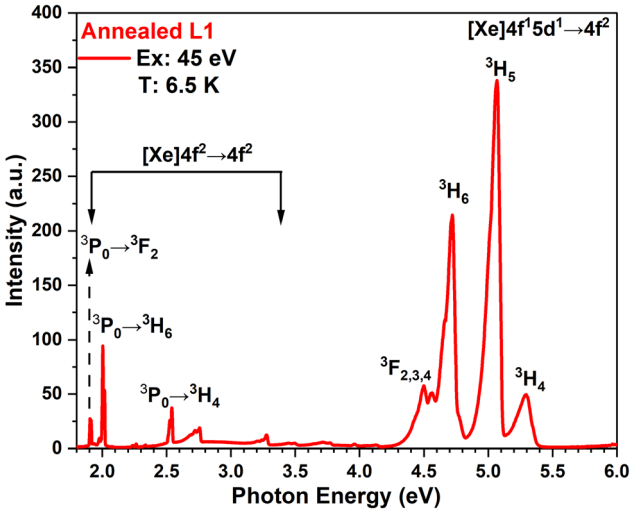

Fig. 6 TI emission spectra of Pr^{3+} doped $LuPO_4$ nanoparticles excited with 45 eV photons at 6.5 K.

$4f^2 \rightarrow 4f^15d^1$ excitation of Pr^{3+} ions and are in agreement with the data already published.[17,47] There are two distinct excitation bands, peaking at 5.41 eV and 6.54 eV, corresponding to the transitions of the first ($[4f5d^1]^1$) and second ($[4f5d^1]^2$) crystal-field components as labeled in ref. 48. In the higher energy region, the features in the excitation spectra are less pronounced, but low intensity peaks near 7 and 7.8 eV can be identified as corresponding to the excitation into the higher d-states ($[4f5d^1]$).[3,4] These peaks are less pronounced or almost absent for the as-prepared samples; however, in general the features of intra-center excitation spectra of the as-prepared and annealed samples are quite similar. For the annealed samples, in full agreement with the literature data,[17,49] the intrinsic absorption starts at 8.5 eV with the exciton creation region, due to electronic excitation formation within the tetrahedral PO_4^{3-} units. The exciton peak energy of 8.8 eV for our samples is in good agreement with the value earlier obtained at 10 K for $LuPO_4$:Pr^{3+} powders.[49] The band gap value can be estimated from the minimum in the excitation spectra shown in Fig. 7. It is equal to 9.2 eV at 7 K, being in good correspondence with the value 9.3 eV obtained for the $LuPO_4$:Nd^{3+} (1%) powder.[43] The process of the excitation of Pr^{3+} ions in the intrinsic absorption region will be discussed in detail in Section 3.2.3. Moreover, the excitation spectra of both as-prepared $LuPO_4$:Pr^{3+} (1%) L1 and L2 samples are completely featureless above 7.5 eV and demonstrate negligible intensity in this region. This is an indication of the absence of energy transfer from the 5d states lying higher than the $[4f5d^1]^2$ component and also from the intrinsic absorption region. To verify this finding, we performed a series of measurements of emission spectra of the as-prepared L1 and L2 samples excited with different photon energies and compared them with the annealed samples as discussed in detail in below sections.

3.2.2. Photoluminescence spectra under the intra-center $4f^2 \rightarrow 4f^15d^1$ excitation of Pr^{3+} ions and excitation in the host absorption region. Fig. 8 presents a comparison of time-integrated PL spectra of the as-prepared and annealed $LuPO_4$:Pr^{3+} (1%) nanocrystals recorded at 6.8 K under intra-center interconfigurational $4f^2 \rightarrow 4f^15d^1$ excitation of the Pr^{3+} ion by the 6.54 eV photons. The PL spectra are normalized in Fig. 8 in order to better compare their structure. Two important features of these spectra have to be mentioned here. First, the annealing process results in the increase of the UV-C emission intensities by a factor of 4 to 7. Second, the emission intensities of both as-prepared and annealed L1 samples are several times weaker compared to the

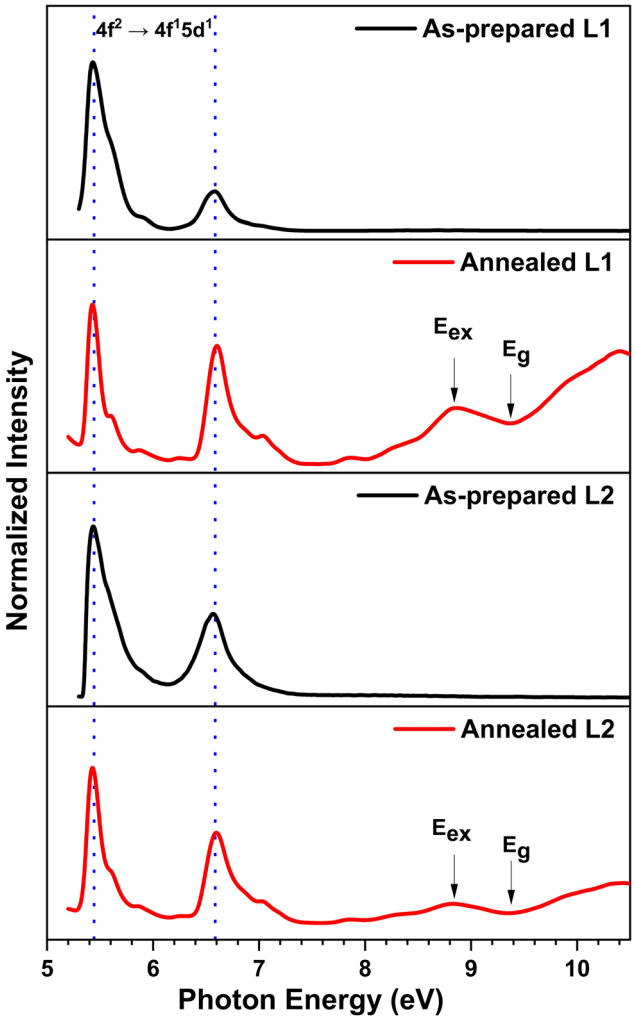

Fig. 7 TI PL excitation spectra of the as-prepared and annealed $LuPO_4:Pr^{3+}$ (1%) nanocrystals at 6.8 K recorded for the $4f^15d^1 \rightarrow {}^3H_5$ luminescence peaked at 5.06 eV (the signal is integrated for the emission energy range from 4.9 to 5.1 eV).

corresponding as-prepared and annealed L2 samples. This difference is attributed to the smaller crystallite size of the as-prepared and annealed L1 samples in comparison with the as-prepared and annealed L2 samples (see Table 3) as well as to short-range disorder providing quenching sites. Apart from this, no significant variation in the spectral positions of the UV-C emission bands was observed for different $LuPO_4:Pr^{3+}$ (1%) nanocrystals, regardless of variations in their size and crystallinity. Since PL spectra of the as-prepared and annealed $LuPO_4:Pr^{3+}$ (1%) nanocrystals demonstrate several excitation bands, as shown in Fig. 7, a detailed study of PL spectra at different exciting photon energies was undertaken to demonstrate the peculiarities of energy transfer from the host to Pr^{3+} ions in the samples synthesized (Fig. 8 and Fig. S2, ESI†).

Fig. 9 and Fig. S2 (ESI†) depict emission spectra recorded under intra-center interconfigurational $4f^2 \rightarrow 4f^15d^1$ excitation of Pr^{3+} ions at 6.54 eV, at the excitation in the host excitonic region at 8.54 eV, as well as in the region of interband transitions at 9.4 and 45 eV. The PL spectra of the annealed $LuPO_4:Pr^{3+}$ (1%) nanocrystals show efficient Pr^{3+} luminescence due to the $4f^15d^1 \rightarrow {}^3H_4$, ${}^3H_5$, ${}^3H_6$, and ${}^3F_{2,3,4}$ ($4f^2$) transitions under excitation in all above-listed energy ranges. However, the Pr^{3+} luminescence intensity is remarkably lower in the as-prepared $LuPO_4:Pr^{3+}$ (1%) nanocrystals, being particularly very weak under excitation in the excitonic region and practically absent under excitation in the fundamental absorption region. These observations are in accordance with the excitation spectra recorded for the as-prepared and annealed $LuPO_4:Pr^{3+}$ (1%) nanocrystals (Fig. 8). The nature of such observations most likely lies in the high degree of local disorder in the as-prepared samples, which is also demonstrated by the Raman spectra (see Fig. 3). The correlation between the Raman and PL excitation spectra is an interesting fact, especially considering that the XRD patterns that are traditionally used to characterize the degree of crystallinity or disorder of the crystal lattice do not show qualitative differences between as-prepared and annealed samples. Our preliminary hypothesis suggests that Raman spectroscopy is much more sensitive to a short-range disorder, mainly related to the rotation or shift of the PO_4 groups from their regular positions. Another possibility is the lowering of the symmetry of the PO_4 group due to protonation,[38] which can

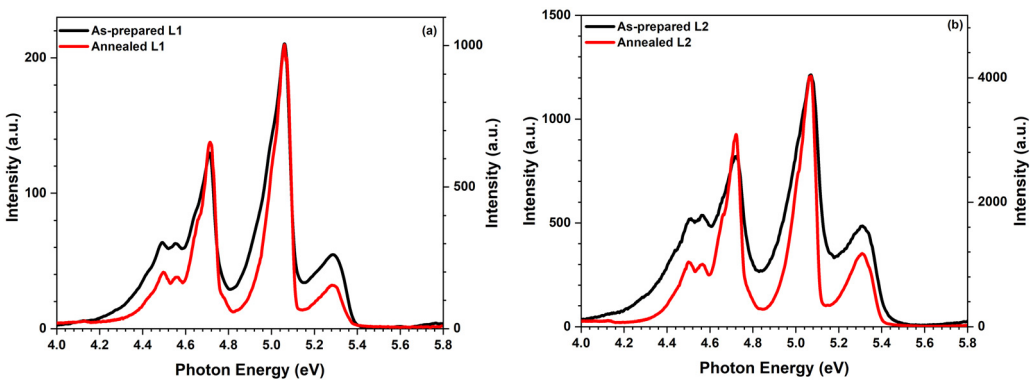

Fig. 8 Effect of annealing on $4f^15d^1 \rightarrow 4f^2$ luminescence intensities of Pr^{3+} ions under intra-center excitation at 6.54 eV of the as-prepared and annealed $LuPO_4:Pr^{3+}$ (1%) nanocrystals at 6.8 K. The intensities of the as-prepared and annealed L1, L2 samples are shown on the left and right intensity axes, respectively.

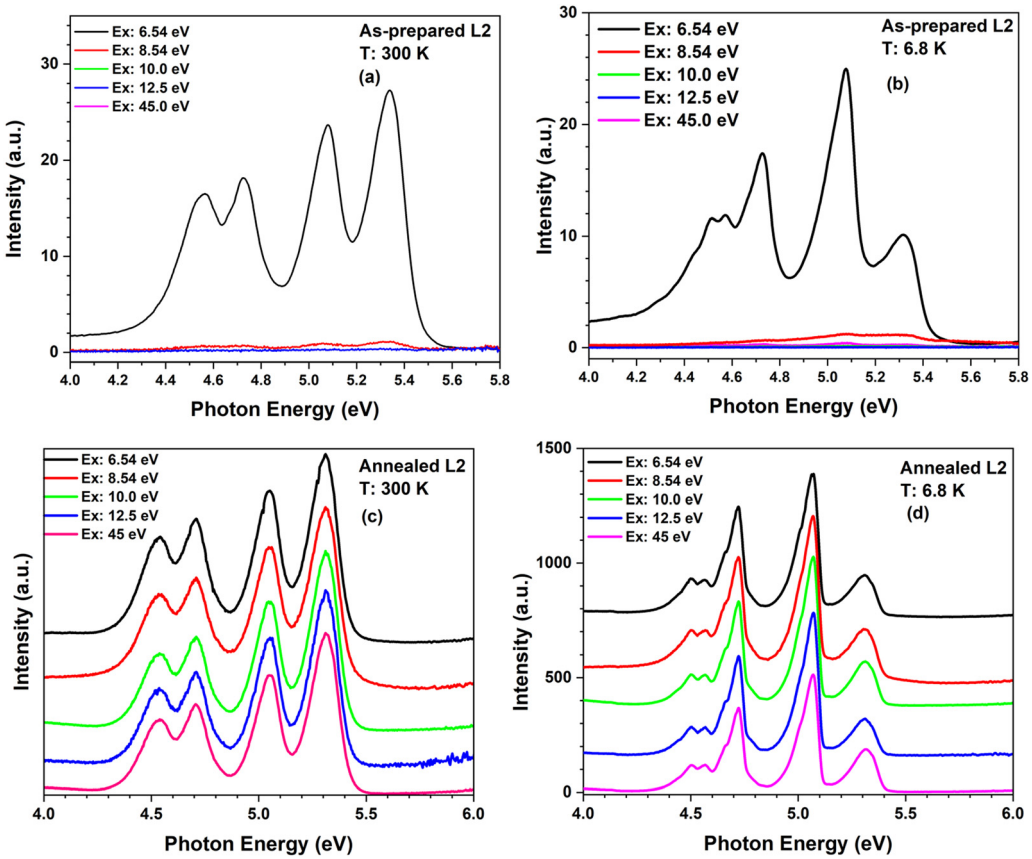

Fig. 9 Pr^{3+} $4f^15d^1 \rightarrow 4f^2$ luminescence spectra of the as-prepared (a) and (b) and annealed (c) and (d) $LuPO_4$:Pr^{3+} (1%) nanocrystals (L2 sample) excited by photons with different energies at 300 and 6.8 K. The luminescence spectra of the annealed sample (c) and (d) are presented as a stacked graph, to better highlight the enhanced luminescence intensity and more distinct spectral features observed under different excitation energies (6.54 to 45 eV). Similar graphs for the L1 sample are shown in Fig. S2 of the ESI† data.

also significantly affect Raman bands. In both scenarios, the annealing procedure would remedy this short-range disorder, enhancing the rearrangement within the crystal lattice and promoting recrystallization. Consequently, the Raman spectra (Fig. 3) and PL excitation spectra (Fig. 7) of the annealed samples exhibit all the expected characteristics of the crystalline $LuPO_4$ material due to the short-range ordering of the crystal lattice and the healing of structural imperfections by annealing. The as-prepared samples are supposed to have a highly disordered lattice, which causes the dispersion of phonon modes of multiple defect sites and their strong broadening, smoothing the Raman spectrum. A direct comparison of phonon energies before and after annealing is not possible, as the as-prepared samples exhibited no Raman-active vibrational modes, while all expected Raman lines appeared after annealing (see Fig. 3 and Table 2). The appearance of Raman lines indicates the improved structural ordering, which also improves energy transfer efficiency and eliminates luminescence quenching centers, as supported by the increased luminescence intensity and lifetime (see Section 3.2.4)

3.2.3. Processes of Pr^{3+} emission excited in the fundamental absorption range. When $LuPO_4$:Pr^{3+} is excited by photons above the band gap energy ($E_g > 9.2$ eV), the Pr^{3+} luminescence occurs *via* a recombination mechanism. In this process, the energy is transferred to the $4f^15d^1$ state of Pr^{3+} ions by thermalized conduction electrons with low kinetic energy and holes created near the top of the valence band. When charge carriers are created near the Pr^{3+} ion by photons with the energy close to the band gap value, their mobility is low, and the capture and recombination of the geminated electron–hole pairs occur at the same Pr^{3+} ion in an extremely fast process.[17] When the excitation energy exceeds noticeably the band gap value, the created charge carriers have higher kinetic energy, resulting in their larger spatial separation and raising the likelihood that they will be captured by the traps induced by impurities or structural imperfections. Shallow traps can also delay the energy transfer to the Pr^{3+} ions, ultimately resulting along with the reduction of luminescence intensity in prolongation of its decay.

In the case of the nanosized $LuPO_4$:Pr^{3+}, the luminescence intensity is strongly influenced by the particle size, crystallinity, structural imperfections (including short-range disorder) and the thermalization length of electrons within the host material, which is typically on order of a few tens of nanometers.[17,50] The structural and morphology studies (XRD, STEM images and Raman spectra shown in Section 3.1) proved that the size of nanocrystals is below the thermalization length of mobile electrons typical of scintillation materials[17,50] in as-prepared

$LuPO_4:Pr^{3+}$ (1%) characterized by the presence of short-range disorder and structural imperfections. These factors increase the probability of non-radiative losses of mobile charge carriers, finally accounting for the reduced luminescence intensity of Pr^{3+} ions in these as-prepared nanocrystals excited in the host absorption region (see Sections 3.2.1 and 3.2.3). Nonetheless, the Pr^{3+} ion emission is still revealed in the as-prepared $LuPO_4:Pr^{3+}$ (1%) nanocrystals excited through the intra-center absorption of the Pr^{3+} ions in the two pronounced lower lying 4f–5d bands peaked at 5.4 and 6.6 eV (Fig. 6). In contrast, the annealing of the $LuPO_4:Pr^{3+}$(1%) nanocrystals reduces significantly the concentration of structural imperfections and increases short-range order, facilitating the appearance of bright Pr^{3+} $4f^15d^1 \rightarrow 4f^2$ luminescence when excited in excitonic and fundamental absorption regions (Fig. 8), which positions the annealed $LuPO_4:Pr^{3+}$(1%) nanocrystals as promising candidates for medical and scintillating applications.

3.2.4. Decay kinetics under intra-center $4f^15d^1 \rightarrow 4f^2$ excitation of Pr^{3+} ions. Fig. 10 shows the decay kinetics curves for different $4f^15d^1 \rightarrow 4f^2$ emission bands recorded for the as-prepared and annealed $LuPO_4:Pr^{3+}$ (1%) nanocrystals under intra-center excitation of the Pr^{3+} ion by the 6.54 eV photons. All decay kinetics monitored for the $4f^15d^1 \rightarrow {}^3H_4$ (5.32 eV), $^3H_5$ (5.06 eV), $^3H_6$ (4.71 eV) transitions deviate from single exponential approximation, though the decay curves can be fitted with two exponential components (Fig. 9). Since these transitions originate from the same excited state of the Pr^{3+} ion, their decay behaviors are inherently related and exhibit similar kinetics. To simplify the analysis and provide a comprehensive understanding of the luminescence properties, the lifetimes (τ_1 and τ_2) of these transitions were averaged to represent the overall decay behavior of the $4f^15d^1 \rightarrow 4f^2$ luminescence (Table 4). The decay components with radiative times τ_1 and τ_2, differing by a factor of at least 3 in all synthesized samples, are ascribed to strongly perturbed and weakly perturbed Pr^{3+} ions within the nanoparticles. The shorter τ_1, associated with strongly perturbed Pr^{3+} ions probably at the nanoparticle surface, dominates in the as-prepared samples, which has a smaller particle size, relatively higher density of structural imperfections and short-range disorders. The τ_1 values of as-prepared L1 and L2 samples are 1.6 ns (97.3%) and 3.2 ns (79.5%), respectively. In contrast, the longer τ_2, corresponding to weakly perturbed Pr^{3+} ions in the bulk of nanoparticles, becomes increasingly prominent after annealing. The τ_2 values of as-prepared L1 and L2 samples are 7.5 ns (2.7%) and 14.5 ns (20.5%) respectively. After annealing at 1000 °C, the decay times for both components become relatively longer, likely due to the removal of non-radiative relaxation pathways, as the annealing reduces structural imperfections and enhances short-range ordering in the Pr^{3+} local environment (as shown in Section 3.1), leading to a shift in the decay dynamics and improved luminescence efficiency. For annealed L1, τ_1 increases to 3.4 ns (61.7%) and τ_2 to 10.6 ns (38.3%), while for L2, τ_1 increases to 5.0 ns (52.6%) and τ_2 to 16.1 ns (47.4%). This redistribution in the decay dynamics indicates a shift from Pr^{3+} ions in strongly perturbing environments, for which τ_1 dominates, to Pr^{3+} ions

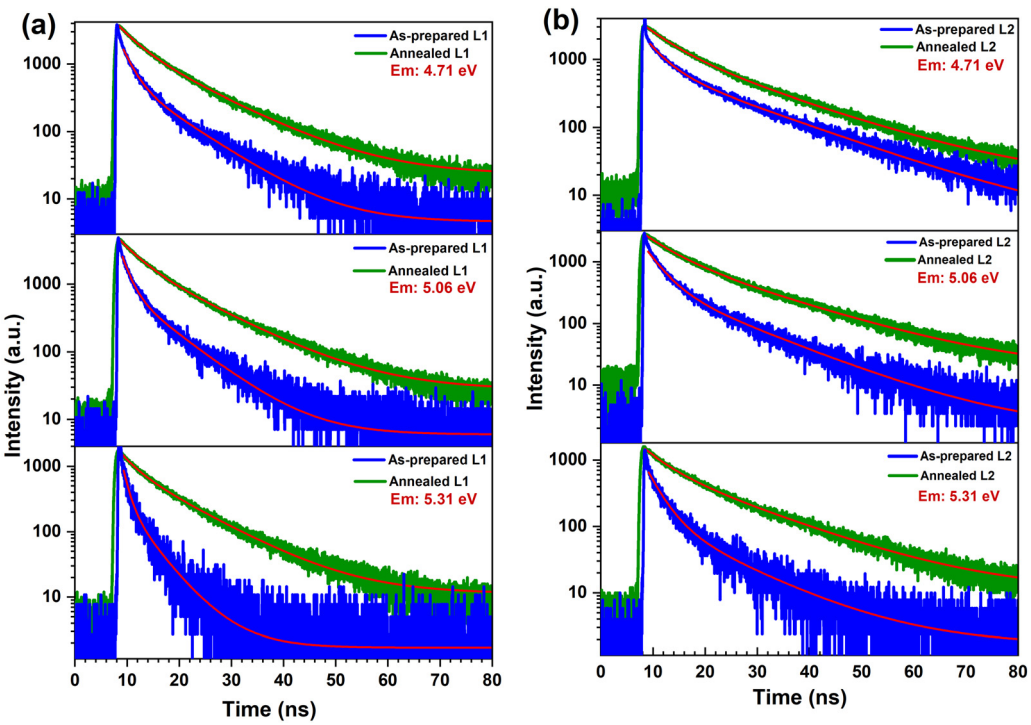

Fig. 10 Effect of annealing on the $4f^15d^1 \rightarrow {}^3H_4$, $^3H_5$, $^3H_6$ luminescence decay of the Pr^{3+} ions for (a) L1 and (b) L2 nanocrystals, recorded under the intra-center excitation of the Pr^{3+} ion by the 6.54 eV photons at 7 K. Experimental data (green and blue lines) are fitted by the bi-exponential decay function, which is shown by red lines. The decay curves are normalized at their maxima for better comparison.

Table 4 Decay times (in ns) and light sums (in %) averaged over the Pr^{3+} $4f^15d^1 \rightarrow {}^3H_{4,5,6}$ emission bands in the UV-C spectral range under intra-center excitation of the studied samples at 7 K

		Radiative transitions (Pr^{3+} $4f^15d^1 \rightarrow {}^3H_{4,5,6}$)	
S. No.	Sample names	τ_1	τ_2
1.	As-prepared L1	1.6 ± 0.3 ns (97.3%)	7.5 ± 0.5 ns (2.7%)
2.	Annealed L1	3.4 ± 0.4 ns (61.6%)	10.6 ± 0.6 ns (38.4%)
3.	As-prepared L2	3.2 ± 0.2 ns (79.5%)	14.4 ± 0.4 ns (20.5%)
4.	Annealed L2	5.0 ± 0.3 ns (52.6%)	16.1 ± 0.5 ns (47.4%)

in weaker perturbing environments characterized by longer τ_2. Additionally, the light sums of both decay components in annealed samples become more comparable, signifying improved luminescence, as the particle size becomes relatively larger and quenching centers become less abundant. The decay times τ_2 observed for the Pr^{3+} emission in the present study are consistent with those reported for other Pr^{3+} doped luminescent materials. For instance, nanocrystalline $LaPO_4$ with particle sizes ranging from 8 to 90 nm exhibited decay times of approximately 9 ns.[51] Similarly, nano- and microcrystalline $LuPO_4$ showed decay times of 11.7 ns ($d \sim$ 20–22 nm) and 11.3 ns ($d \sim$ 6.5 μm), respectively,[17] while nanocrystalline $LuPO_4$ ($d \sim$ 35 nm) displayed a decay time of 7 ns.[7] The shorter decay times of as-prepared $LuPO_4$:Pr^{3+} samples, caused by a smaller particle size, higher structural imperfection and short range disorder, are mitigated through annealing, resulting in the redistributed intensities of decay components, and thus, improved light characteristics and enhancing their potential for efficient and stable luminescence applications.

3.3. Time-resolved photoluminescence spectroscopy of the as-prepared $LuPO_4$:Pr^{3+} (1%) nanocrystals under synchrotron radiation excitation

Building on the insights gained from the decay kinetics, we studied the time-resolved excitation spectra of as-prepared samples to further explore the relaxation dynamics of the Pr^{3+} $4f^15d^1 \rightarrow 4f^2$ luminescence. These spectra provide critical information about the fast and slow relaxation processes associated with strongly and weakly perturbed Pr^{3+} ions. By leveraging synchrotron radiation excitation, it becomes possible to probe relaxation dynamics within the nanosecond time range as demonstrated in Pr^{3+} doped $BaLuF_5$ nanoparticles.[52] To investigate these relaxation processes in $LuPO_4$:Pr^{3+} (1%) nanocrystals, the time-resolved PL excitation spectra of the $4f^15d^1 \rightarrow {}^3H_5$ luminescence (5.06 eV) were recorded at 7 K using synchrotron radiation at FinEstBeAMS. The detailed methods for measuring, plotting, and analyzing the TR excitation spectra are provided in ref. 52. The excitation spectra are shown in two time-windows, short and long, marked as STW (δt = 0 and Δt = 4 ns) and LTW (δt = 4 and Δt = 20 ns), respectively, which are selected based on decay kinetics studies (see Fig. 9) to distinguish the faster relaxation processes, dominated by strongly perturbed Pr^{3+} ions, from the slower processes, characteristic of weakly perturbed Pr^{3+} ions. The time δt = 0 ns is defined by the arrival of the VUV excitation pulse, and the luminescence signal is integrated over Δt = 4 ns in the STW. In the LTW, the integration over Δt = 20 ns starts at δt = 4 ns after the excitation pulse (Fig. 11).

The excitation spectra recorded in the two-time windows reveal clearly visible differences. In the STW, the $4f^2 \rightarrow 4f^15d^1$ excitation bands exhibit a redshift of approximately 0.038 eV for L1 and 0.03 eV for L2 compared to the $4f^2 \rightarrow 4f^15d^1$ excitation bands in the LTW, which remain at relatively higher energies. This redshift in the STW is attributed to strongly perturbed Pr^{3+} ions probably situated near the nanoparticle surface, where structural imperfections and short-range disorder dominate. Conversely, the LTW spectra reflect weakly perturbed Pr^{3+} ions located in the bulk of the nanoparticles, where the influence of surface effects is significantly reduced. In the excitonic excitation region, the STW spectra show a blueshift of approximately 0.19 eV for both L1 and L2 compared to the LTW spectra. This opposite trend highlights the contrasting behavior of excitonic states in the strongly disordered crystal region with respect to that of the $4f^15d^1$ states, further emphasizing the role of structural and morphological variations in energy transfer processes.

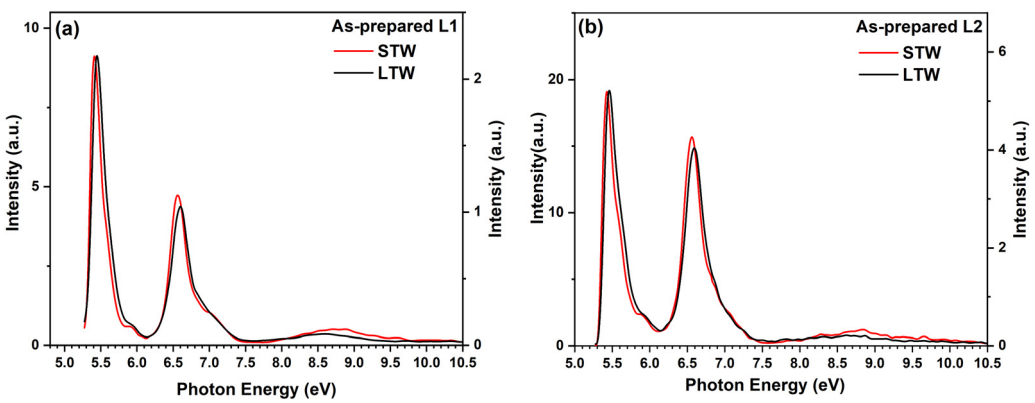

Fig. 11 Time resolved PL excitation spectra of the as-prepared $LuPO_4$:Pr^{3+} (1%) L1 (a) and L2 (b) nanocrystals recorded at 6.8 K for the $4f^15d^1 \rightarrow {}^3H_5$ luminescence at 5.06 eV in the STW (δt = 0 and Δt = 4 ns) and LTW (δt = 4 and Δt = 20 ns). The spectra are normalized to the highest intensity of the excitation band for better comparison.

Thus, in conclusion, the time-resolved PL excitation spectra provide a comprehensive understanding of the relaxation dynamics in $LuPO_4$:Pr^{3+} nanocrystals. The observed spectral shifts and trends confirm the strong influence of structural imperfections and crystallinity on the Pr^{3+} luminescence, with annealing treatments offering a promising approach to mitigate these imperfections. By reducing the disorder rate and enhancing energy transfer efficiency, annealing significantly improves the luminescence efficiency of $LuPO_4$:Pr^{3+} nanocrystals, making them highly suitable for advanced luminescence applications.

Conclusions

This study highlights the pivotal role of local structural disorder in influencing the energy transfer processes and luminescence properties of $LuPO_4$:Pr^{3+} nanocrystals. The high degree of short-range disorder in the as-prepared nanocrystals, undetected by XRD, was found to impair energy transfer between the host lattice and Pr^{3+} ions, suppressing luminescence excitation through the host-to-ion transfer. A significant outcome of this work is the observation of bright Pr^{3+} $4f^15d^1 \rightarrow 4f^2$ emissions in annealed nanocrystals, positioning these materials as promising candidates for medical and optical applications. It is important to note that excitation by high-energy 45 eV photons in the deep fundamental absorption of $LuPO_4$ results in UV-C emissions, demonstrating that analogous energy conversion is expected in radiotherapy treatment. Through decay kinetics and time-resolved excitation spectroscopy, this study further identified the presence of two distinct Pr^{3+} ion environments, which are strongly perturbed Pr^{3+} ions located at the nanoparticle surface and weakly perturbed Pr^{3+} ions situated in the bulk of the nanoparticles. Our research also showed that Raman spectroscopy proved to be a practical and informative tool for characterizing nanomaterials synthesized at low temperatures, clarifying the contradiction in the results provided by XRD and luminescence spectroscopy for as-prepared and annealed nanocrystals. Raman spectroscopy clearly showed that thermal annealing of our nanocrystals drastically improved the local ordering in the crystal lattice, resulting in significantly improved UV-C luminescence intensity. These findings highlight the importance of post-synthesis treatment in optimizing the performance of nanocrystals for practical applications, particularly in the biomedical field and other high-performance applications.

Data availability

All data supporting the findings of this study are included within the article and its ESI,† ensuring transparency and reproducibility. Additional raw datasets generated during this study are available from the corresponding author upon reasonable request. On behalf of all co-authors, we affirm our commitment to facilitating the accessibility and integrity of the data presented in this work, contributing to the advancement of scientific knowledge.

Conflicts of interest

There are no conflicts to declare.

Acknowledgements

We would like to thank the MAX IV Lab staff for their valuable contribution to our research. We are also grateful to Dr Tavo Romann and Dr Valter Kiisk for their assistance with the Raman experiments. The financial support from the GSFMT Graduate School, Estonian Research Council (grant PRG629) and Center of Excellence (TK 210) is gratefully acknowledged. We acknowledge the MAX IV Laboratory for the beamtime on the FinEstBeAMS beamline under Proposal 20211020 and 20221357. Research conducted at MAX IV, a Swedish national user facility, is supported by the Swedish Research Council under contract 2018-07152, the Swedish Governmental Agency for Innovation Systems under contract 2018-04969, and Formas under contract 2019-02496. The activities of Estonian researchers at the FinEstBeAMS beamline of the MAX IV Lab were partially funded within the MAX-TEENUS project (grant no. 2014-2020.4.01.20-0278 by the ERDF funding in Estonia granted to the University of Tartu) and by the Estonian Research Council project TT20.

References

1 R. Baskar, K. A. Lee, R. Yeo and K.-W. Yeoh, *Int. J. Med. Sci.*, 2012, **9**, 193–199.
2 T. L. de Jager, A. E. Cockrell and S. S. Du Plessis, in *Ultraviolet Light in Human Health, Diseases and Environment*, ed. S. I. Ahmad, Springer International Publishing, Cham, 2017, vol. 996, pp. 15–23.
3 M. R. Squillante, T. Jüstel, R. R. Anderson, C. Brecher, D. Chartier, J. F. Christian, N. Cicchetti, S. Espinoza, D. R. McAdams, M. Müller, B. Tornifoglio, Y. Wang and M. Purschke, *Opt. Mater.*, 2018, **80**, 197–202.
4 B. Poljšak and R. Dahmane, *Dermatol. Res. Pract.*, 2012, 1–4.
5 I. Villa, C. Villa, R. Crapanzano, V. Secchi, M. Tawfilas, E. Trombetta, L. Porretti, A. Brambilla, M. Campione, Y. Torrente, A. Vedda and A. Monguzzi, *ACS Appl. Mater. Interfaces*, 2021, **13**, 12997–13008.
6 S. Miwa, S. Yano, Y. Hiroshima, Y. Tome, F. Uehara, S. Mii, E. V. Efimova, H. Kimura, K. Hayashi, H. Tsuchiya and R. M. Hoffman, *J. Cell. Biochem.*, 2013, **114**, 2493–2499.
7 V. Vistovskyy, T. Malyi, A. Vas'kiv, M. Chylii, N. Mitina, A. Zaichenko, A. Gektin and A. Voloshinovskii, *J. Lumin.*, 2016, **179**, 527–532.
8 M. Müller, S. Espinoza, T. Jüstel, K. D. Held, R. R. Anderson and M. Purschke, *Radiat. Res.*, 2019, **193**, 82.
9 T. M. Allen and P. R. Cullis, *Science*, 2004, **303**, 1818–1822.
10 G. Tiwari, R. Tiwari, S. Bannerjee, L. Bhati, S. Pandey, P. Pandey and B. Sriwastawa, *Int. J. Pharm. Invest.*, 2012, **2**, 2.
11 B. Yu, H. C. Tai, W. Xue, L. J. Lee and R. J. Lee, *Mol. Membr. Biol.*, 2010, **27**, 286–298.
12 R. Singh and J. W. Lillard, *Exp. Mol. Pathol.*, 2009, **86**, 215–223.

13 H. M. Redhead, S. S. Davis and L. Illum, *J. Controlled Release*, 2001, **70**, 353–363.
14 H. Li, X. Pu, J. Yin, X. Wang, S. Yao, H. M. Noh and J. H. Jeong, *J. Am. Ceram. Soc.*, 2016, **99**, 954–961.
15 Y. Asscher, G. Dal Sasso, L. Nodari, I. Angelini, T. Boffa Ballaran and G. Artioli, *Phys. Chem. Chem. Phys.*, 2017, **19**, 21783–21790.
16 A. O. Shilov, R. V. Kamalov, M. S. Karabanalov, A. V. Chukin, A. S. Vokhmintsev, G. B. Mikhalevsky, D. A. Zamyatin, A. M. A. Henaish and I. A. Weinstein, *Nanomaterials*, 2023, **13**, 3109.
17 J. Kappelhoff, J.-N. Keil, M. Kirm, V. N. Makhov, K. Chernenko, S. Möller and T. Jüstel, *Chem. Phys.*, 2022, **562**, 111646.
18 S. Espinoza, M. Volhard, H. Kätker, H. Jenneboer, A. Uckelmann, M. Haase, M. Müller, M. Purschke and T. Jüstel, *Part. Part. Syst. Charact.*, 2018, **35**, 1800282.
19 H. Mändar, J. Felsche, V. Mikli and T. Vajakas, *J. Appl. Crystallogr.*, 1999, **32**, 345–350.
20 H. Mändar, T. Vajakas, J. Telsche and R. E. Dinnebier, *J. Appl. Crystallogr.*, 1996, **29**, 304.
21 A. Niilisk, T. Kahro, V. Kiisk, M. Rähn, H. Alles, J. Aarik and V. Sammelselg, *Open Phys.*, 2015, **13**, 34–40.
22 M. Visnapuu, M. Rosenberg, E. Truska, E. Nõmmiste, A. Šutka, A. Kahru, M. Rähn, H. Vija, K. Orupõld, V. Kisand and A. Ivask, *Colloids Surf., B*, 2018, **169**, 222–232.
23 M. Rosenberg, M. Visnapuu, K. Saal, D. Danilian, R. Pärna, A. Ivask and V. Kisand, *Nanomaterials*, 2021, **11**, 3384.
24 R. Pärna, R. Sankari, E. Kukk, E. Nõmmiste, M. Valden, M. Lastusaari, K. Kooser, K. Kokko, M. Hirsimäki, S. Urpelainen, P. Turunen, A. Kivimäki, V. Pankratov, L. Reisberg, F. Hennies, H. Tarawneh, R. Nyholm and M. Huttula, *Nucl. Instrum. Methods Phys. Res., Sect. A*, 2017, **859**, 83–89.
25 K. Chernenko, A. Kivimäki, R. Pärna, W. Wang, R. Sankari, M. Leandersson, H. Tarawneh, V. Pankratov, M. Kook, E. Kukk, L. Reisberg, S. Urpelainen, T. Käämbre, F. Siewert, G. Gwalt, A. Sokolov, S. Lemke, S. Alimov, J. Knedel, O. Kutz, T. Seliger, M. Valden, M. Hirsimäki, M. Kirm and M. Huttula, *J. Synchrotron Radiat.*, 2021, **28**, 1620–1630.
26 V. Pankratov, R. Pärna, M. Kirm, V. Nagirnyi, E. Nõmmiste, S. Omelkov, S. Vielhauer, K. Chernenko, L. Reisberg, P. Turunen, A. Kivimäki, E. Kukk, M. Valden and M. Huttula, *Radiat. Meas.*, 2019, **121**, 91–98.
27 J. Saaring, A. Vanetsev, K. Chernenko, E. Feldbach, I. Kudryavtseva, H. Mändar, R. Pärna, V. Nagirnyi, S. Omelkov, I. Romet, O. Rebane and M. Kirm, *J. Alloys Compd.*, 2021, **883**, 160916.
28 S. I. Omelkov, K. Chernenko, J. C. Ekström, A. Jurgilaitis, A. Khadiev, A. Kivimäki, A. Kotlov, D. Kroon, J. Larsson, V. Nagirnyi, D. V. Novikov, V.-T. Pham, R. Pärna, I. Romet, J. Saaring, I. Schostak, E. Tiirinen, A. Tõnisoo and M. Kirm, *J. Phys.: Conf. Ser.*, 2022, **2380**, 012135.
29 P. Li, Y. Liu, Y. Guo, X. Shi, G. Zhu and H. Zuo, *Ceram. Int.*, 2015, **41**, 6620–6630.
30 X. Zhang, M. Zhang, Y. Zhu, P. Wang, F. Xue, J. Gu, H. Bi and Y. Qian, *Mater. Res. Bull.*, 2010, **45**, 1324–1329.
31 Y. Zhang and H. Guan, *J. Cryst. Grow.*, 2003, **256**, 156–161.
32 Y. Ni, J. M. Hughes and A. N. Mariano, *Am. Mineral.*, 1995, **80**, 21–26.
33 R. D. Shannon, *Acta Crystallogr., Sect. A:Found. Adv.*, 1976, **32**, 751–767.
34 A. Debelle, A. Boulle, A. Chartier, F. Gao and W. J. Weber, *Phys. Rev. B:Condens. Matter Mater. Phys.*, 2014, **90**, 174112.
35 S. Loridant, *Catal. Today*, 2021, **373**, 98–111.
36 W. O. Milligan, D. F. Mullica, G. W. Beall and L. A. Boatner, *Inorg. Chim. Acta*, 1982, **60**, 39–43.
37 A. Sanson, M. Giarola, M. Bettinelli, A. Speghini and G. Mariotto, *J. Raman Spectrosc.*, 2013, **44**, 1411–1415.
38 G. Gouadec and P. Colomban, *Prog. Cryst. Growth Charact. Mater.*, 2007, **53**, 1–56.
39 R. Javed, M. Zia, S. Naz, S. O. Aisida, N. U. Ain and Q. Ao, *J. Nanobiotechnol.*, 2020, **18**, 172.
40 R. P. Bagwe, L. R. Hilliard and W. Tan, *Langmuir*, 2006, **22**, 4357–4362.
41 P. Dorenbos, *Phys. Rev. B:Condens. Matter Mater. Phys.*, 2012, **85**, 165107.
42 A. M. Srivastava, *J. Lumin.*, 2016, **169**, 445–449.
43 V. N. Makhov, N. Y. Kirikova, M. Kirm, J. C. Krupa, P. Liblik, A. Lushchik, C. Lushchik, E. Negodin and G. Zimmerer, *Nucl. Instrum. Methods Phys. Res., Sect. A*, 2002, **486**, 437–442.
44 Y. Takebuchi, M. Koshimizu, K. Ichiba, T. Kato, D. Nakauchi, N. Kawaguchi and T. Yanagida, *Materials*, 2023, **16**, 4502.
45 W. T. Carnall, G. L. Goodman, K. Rajnak and R. S. Rana, *J. Chem. Phys.*, 1989, **90**, 3443–3457.
46 I. Romet, É. Tichy-Rács, K. Lengyel, E. Feldbach, L. Kovács, G. Corradi, K. Chernenko, M. Kirm, D. Spassky and V. Nagirnyi, *J. Lumin.*, 2024, **265**, 120216.
47 A. M. Srivastava, M. Jennings and J. Collins, *Opt. Mater.*, 2012, **34**, 1347–1352.
48 A. M. Srivastava, A. A. Setlur, H. A. Comanzo, W. W. Beers, U. Happek and P. Schmidt, *Opt. Mater.*, 2011, **33**, 292–298.
49 V. V. Mikhailin, D. A. Spassky, V. N. Kolobanov, A. A. Meotishvili, D. G. Permenov and B. I. Zadneprovski, *Radiat. Meas.*, 2010, **45**, 307–310.
50 Z. Wang, Y. Xie, L. W. Campbell, F. Gao and S. Kerisit, *J. Appl. Phys.*, 2012, **112**, 014906.
51 T. S. Malyy, V. V. Vistovskyy, Z. A. Khapko, A. S. Pushak, N. E. Mitina, A. S. Zaichenko, A. V. Gektin and A. S. Voloshinovskii, *J. Appl. Phys.*, 2013, **113**, 224305.
52 S. B. Maji, A. Vanetsev, H. Mändar, V. Nagirnyi, K. Chernenko and M. Kirm, *Opt. Mater.*, 2024, **154**, 115781.